Available online at www.sciencedirect.com
ScienceDirect
Earth and Planetary Science Letters 262 (2007) 543–551
EPSL
www.elsevier.com/locate/epsl

Chemical imaging with NanoSIMS: A window into deep-Earth geochemistry

James Badro [a,b,c,*], Frederick J. Ryerson [c], Peter K. Weber [d], Angèle Ricolleau [a,b], Stewart J. Fallon [d], Ian D. Hutcheon [d]

[a] *IMPMC, Université Pierre et Marie Curie, CNRS, Paris, France*
[b] *Minéralogie, Institut de physique du globe de Paris, CNRS, Paris, France*
[c] *Energy and Environment, Lawrence Livermore National Laboratory, Livermore, California, USA*
[d] *Chemistry and Materials Science, Lawrence Livermore National Laboratory, Livermore, California, USA*

Received 2 March 2007; received in revised form 17 July 2007; accepted 11 August 2007
Available online 22 August 2007
Editor: G.D. Price

Abstract

We use a combination of nanometer-resolution secondary ion mass spectrometry (NanoSIMS) and analytical transmission electron microscopy (ATEM) for chemical imaging of material transformed in a laser-heated diamond anvil cell (LH-DAC), in the pressure and temperature range of Earth's lower mantle. MORB (mid-ocean ridge basalt), one of the components of subducted oceanic lithosphere, was transformed to an assemblage of Mg-perovskite, Ca-perovskite, stishovite and a calcium ferrite-structure phase at 55 GPa and 2100 °C in an LH-DAC. Elemental imaging spanning the entire range of concentrations, from major elements such as silicon (49.5 wt.% SiO_2) to trace elements such as strontium (118 ppm), scandium, and yttrium (both at 40 ppm) was obtained with a Cameca NanoSIMS 50. We observe a preferential partitioning of scandium, yttrium and strontium in the calcium silicate perovskite phase, and we compare this to recently measured solid–liquid partition coefficients and fractionation at lower pressures. This type of measurement demonstrates that even the most complex mineral assemblages can be probed using this combination of techniques and opens new pathways towards the characterization and quantification of geochemical interactions and processes occurring in the deep Earth.

Keywords: lower mantle; geochemistry; trace elements; petrology; diamond anvil cell; laser heating; nanoSIMS

1. Introduction

Characterizing the processes that control the chemical and isotopic variability of the Earth's interior is an important component in understanding the dynamical evolution of the planet. It is based on input from multiple sources of geochemical data collected at the surface, as well as those representative of chemical processes occurring at various depths. Hotspot volcanism and kimberlitic xenoliths, are thought to originate at least partially from the lower mantle (Madureira et al., 2005), and could even bear the signature of core–mantle interactions (Walker et al., 1995; Brandon and Walker, 2005). Attempts to understand the chemical evolution on a global scale must consider chemical interactions within the deep Earth — the lower mantle and core. However,

* Corresponding author. IMPMC, Université Pierre et Marie Curie, CNRS, Paris, France.
E-mail address: badro@ipgp.jussieu.fr (J. Badro).

0012-821X/$ - see front matter © 2007 Elsevier B.V. All rights reserved.
doi:10.1016/j.epsl.2007.08.007

most partitioning measurements have been limited to samples transformed in piston-cylinder devices, and more recently in multi-anvil devices (Righter, 2003; Corgne et al., 2005; Liebske et al., 2005 and references therein). The latter are capable of covering the pressure and temperature range of the upper mantle, but are not suitable to probe lower mantle conditions ($P>24$ GPa, $T>2500$ °C), leaving most of the Earth's deep interior free of experimental constraints. Therefore, geochemical models of lower-mantle interactions are necessarily extrapolated from lower pressure and temperature measurements, and cannot take into account the effects of structural phase transitions (e.g. Fiquet, 2001; Murakami et al., 2004) and spin-state transitions (e.g. Badro et al., 2003, 2004; Sturhahn et al., 2005; Speziale et al., 2005) that occur at higher pressure and temperature. Here, we demonstrate that coupling experiments performed in the laser-heated diamond anvil cell (LH-DAC) with microscopic sample extraction techniques (Focused Ion Beam — FIB), analytical transmission electron microscopy (ATEM) and nanometer-resolution secondary ion mass spectrometry (NanoSIMS), is capable of extending elemental partitioning investigations to lower-mantle conditions.

2. Experimental and analytical techniques

A thin slab (60 μm side, 10 μm thick) of unaltered, natural MORB pillow glass (East Pacific Rise), was compressed in a diamond anvil cell using neon (soft and inert) as a pressure medium. The sample was heated and transformed *in situ* by laser-heating using two single-mode (TEM_{00}) Nd:YAG infrared lasers (40 W each), with a hotspot size of 30 μm, for 15 min at 2100 °C and 55 GPa. The sample was quenched, decompressed, and recovered for analysis (Ricolleau et al., submitted for publication).

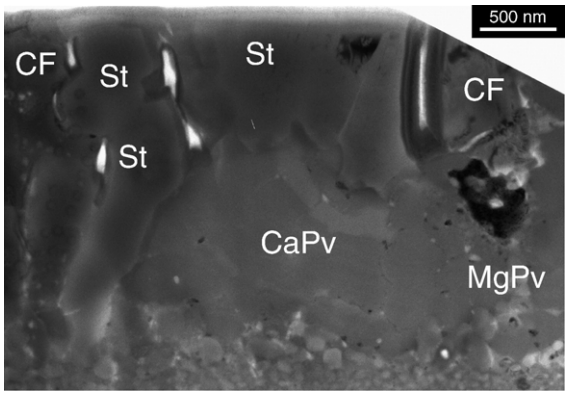

Fig. 1. Scanning TEM bright-field image of the FIB thin section showing the grains of magnesium perovskite (*MgPv*), calcium perovskite (*CaPv*), stishovite (*St*), calcium ferrite-type phase (*CF*). The area of this image corresponds to the grey square on the SIMS image in Fig. 3.

Table 1
Major-element composition of MORB and mineral phases in DAC-transformed MORB, obtained by EDX ATEM measurement

wt.%	MORB	*MgPv*	*CaPv*	*St*	*CF*
SiO_2	49.74 (0.49)	40.9 (0.6)	52.1 (0.2)	98.5 (0.4)	26.7 (0.4)
TiO_2	1.33 (0.13)	2.1 (0.2)	1.2 (0.1)	0.1 (0.1)	0.2 (0.1)
Al_2O_3	15.89 (0.23)	23.6 (0.9)	2.5 (0.7)	0.9 (0.1)	43.2 (1.3)
FeO	9.73 (0.28)	10.1 (0.5)	3.5 (0.6)	0.1 (0.1)	6.2 (1.1)
MgO	8.46 (0.12)	19.1 (0.6)	3.9 (1.1)	0.1 (0.1)	12.9 (1.7)
CaO	11.74 (0.19)	3.3 (0.3)	36.8 (2.5)	0.4 (0.3)	1.7 (0.6)
Na_2O	2.69 (0.09)	0.8 (0.2)	0.1 (0.1)	0.0 (0.0)	9.1 (0.2)

Numbers in parentheses represent the standard error.

The sample was removed from the DAC chamber, and placed on a conducting carbon tape attached to an SEM sample holder for FIB milling (Heaney et al., 2001; Reusser et al., 2003; Irifune et al., 2005). We used an FEI Model 200 TEM FIB system at the University of Aix-Marseille (France). A thin layer of platinum was deposited on top of the region of interest in order to prevent surface degradation. A thin section was obtained using a 30 kV Ga^+ beam operating at ~20 nA, as we excavated the sample from both sides of the Pt layer to a depth of ~5 μm. The sample was further thinned to ~200 nm with a beam current of ~100 pA and by tilting the sample by 1.2°. Last, a line pattern was milled with the ion beam along the sides and bottom edges of the thin section, setting it loose from the rest of the sample (see Ricolleau et al., submitted for publication for a complete description). The thin section (size of ~20 μm × ~5 μm × ~200 nm) was removed using a stereomicroscope and a hydraulic micromanipulator, and placed onto a membrane of carbon-coated 200-mesh copper grid.

Electron microscopy, diffraction and major element chemical analysis of the section were conducted on a JEOL JEM 2100F UHR ATEM at Université Pierre et Marie Curie (Paris, France) and a Phillips CM30 ATEM at Université des Sciences et Technologie de Lille (Lille, France). The transformed sample consists of four phases (Fig. 1): magnesium and calcium silicate perovskites (*MgPv* and *CaPv*, respectively), stishovite (*St*), and a calcium-ferrite structure Al-rich silicate (*CF*). The major-element composition of each phase was determined by energy-dispersive X-ray analysis (EDX), and is given in Table 1. The K factors (Cliff and Lorimer, 1975) were determined experimentally for all elements of interest, following the method of Vancappellen (1990). For the absorption correction, we adjusted (Vancappellen and Doukhan, 1994) the thickness parameter in the quantification program until the resultant composition satisfied

electroneutrality. EDX analyses were performed in scanning mode using a 50×50 nm window to avoid amorphisation and to prevent the volatilisation of alkali ions. When the grains were smaller, the probe size was reduced to about 10 nm.

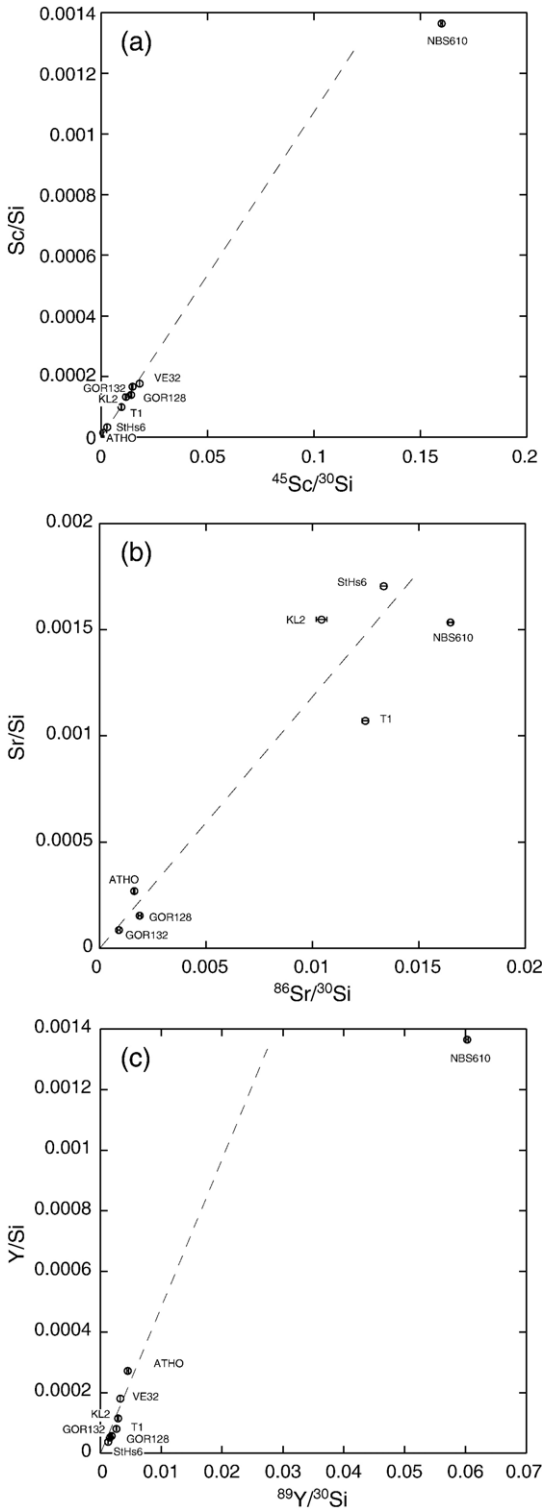

Fig. 2. Measured $^{45}Sc/^{30}Si$, $^{86}Sr/^{30}Si$ and $^{89}Y/^{30}Si$ on the nanoSIMS as a function of actual Si-normalised composition (Sc/Si, Sr/Si and Y/Si) for a suite of glass standards (Jochum et al., 2000) define the working curves used for quantification. These include geologically relevant compositions ranging from komatiite (GOR128, GOR132), basalts (KL2), andesite (StHs6), tonalite (T1) to granite (ATHO). In addition, NBS610 and the starting material (VE32) are also reported. The relative sensitivity factors (RSFs) were obtained by a linear regression forced through zero (dashed lines). The standard error is that of the slope of the regression curve and is propagated in all subsequent concentration data.

The section was then sputter-coated with gold for SIMS analysis. SIMS was performed using the multi-collector Cameca NanoSIMS 50 instrument at Lawrence Livermore National Laboratory (Livermore, CA). A ~5 pA O^- primary beam was focused to a nominal spot size of ~200 nm and rastered over 256×256 or 128×128 pixel regions to generate secondary ions for quantification. Dwell time was 2 to 5 ms/pixel, and raster size was 3 to 5 μm^2. The sputtering rate is ~0.15 nm μm^2/pA/s, corresponding to an effective sputtering depth of 2.5 nm per pass. Secondary ion mass spectrometry was performed without energy filtering at a mass resolving power of 4000. Having selected the elements of interest, along with those required for normalization, specific isotopes are chosen based upon the working mass resolution and that required to resolve known isobaric interferences. For instance, the interference between $^{29}Si^{16}O$ interference on ^{45}Sc requires a mass resolution of 2900, and would require energy filtering to minimise the oxide intensity coupled with peak deconvolution when analysed with a low mass resolution instrument. The ability to obtain high sensitivity at high mass resolution ameliorates this issue. In addition, when working with a static magnetic field in multi-collection mode, the selection of any group of analysed masses is constrained by the physical separation of the detectors. If the heaviest investigated ion has $Z<34$, one mass unit separation can be obtained between two consecutive detectors. But higher mass separation is required if $Z>34$. Hence, it is not possible to measure concomitantly ^{27}Al and ^{28}Si; when ^{27}Al was analysed, ^{29}Si or ^{30}Si were probed. Similarly, analysing Na and Al (both monoisotopic) concomitantly with Mg (exists naturally as ^{24}Mg, ^{25}Mg, and ^{26}Mg) forces the choice of ^{25}Mg, which provides the only combination that is more than one mass unit away from both ^{23}Na and ^{27}Al. We did not use automated magnetic field changes to switch between species during the course of the analysis, which is another option for solving this problem.

Analysis was performed in static, multi-collection mode for a series of five secondary ions suites [$^{23}Na^+$,

$^{27}Al^+$, $^{29}Si^+$, $^{40}Ca^+$, $^{56}Fe^+$], [$^{23}Na^+$, $^{27}Al^+$, $^{29}Si^+$, $^{48}Ti^+$, $^{56}Fe^+$], [$^{24}Mg^+$, $^{27}Al^+$, $^{30}Si^+$, $^{45}Sc^+$, $^{89}Y^+$], and [$^{23}Na^+$, $^{28}Si^+$, $^{40}Ca^+$, $^{88}Sr^+$, $^{138}Ba^+$] by pulse counting on individual electron multipliers. 10 to 20 serial quantitative secondary ion images (layers) were generated for each suite. The data were processed as quantitative isotopic images normalized to the intensity of a major element (^{28}Si, ^{29}Si, and ^{30}Si) using the Limage software package (Larry Nittler, Carnegie Institution of Washington, DC, USA). Secondary ion intensities were corrected for detector dead time and image shift from layer to layer, and normalized to silicon. Domains corresponding to individual phases and grains were defined as regions of interest (ROIs), and the normalized secondary ion intensities for each ROI was calculated by averaging over all of the replicate layers. Quantitative analysis is achieved by correcting the normalized secondary ion intensities with relative useful yields obtained from standards under identical analysis conditions.

Relative sensitivity factors (RSFs) were determined using the working curve in which the ^{30}Si-normalized intensity of the isotopes of interest, ^{45}Sc, ^{86}Sr and ^{89}Y were obtained for samples of different compositions (Fig. 2). Here we used a suite of glass standard prepared by Jochum et al. (2000) that include geologically relevant compositions ranging from komatiite (GOR128, GOR132), basalts (KL2), andesite (StHs6), tonalite (T1) to granite (ATHO). In addition, we also collected data for NBS610 (a high silica, 72 wt.%, sodium, calcium aluminosilicate glass standard containing ~500 ppm of various trace elements) and the glassy starting material (VE32) used in this experiment. The RSFs were obtained by linear regression of the Si-normalized intensity of each isotope and its Si-normalized composition. The regression was forced through zero and the standard error is that of the slope of the regression curve and is propagated in all subsequent concentration data (Table 2).

It is well known that RSFs can vary as a function of matrix composition. In many cases, this matrix effect can be ameliorated by energy filtering (Hinton, 1990). Energy filtering is not currently in routine use on the NanoSIMS, and was not attempted here. The most obvious matrix effects concern the secondary ion yields from NBS610. The linear regression in Fig. 2 does not include the NBS610 data which clearly fall off the trend defined by the "geologic standards". This is most apparent in the Y/Si *vs* $^{89}Y/^{30}Si$ data (Fig. 2c). The RSF for Y with and without inclusion of the NBS610 result vary approximately a factor of two, while those for Sc and Sr, by ~21% and ~9%, respectively. Omitting the NBS610 data from the regression yields standard errors of regression of less than 10%, indicating the matrix effects for these elements along the compositional vector defined by our standards is reasonably good for this application. That NBS610 is not in such good agreement may owe to its compositional simplicity, devoid of elements such as Mg and Fe. We use the RSFs excluding the NBS610 data in subsequent quantification. Calibration data for ^{86}Sr were corrected for isotopic composition when applied to quantification of ^{88}Sr data for the LH-DAC transformed sample.

Table 2
Relative sensitivity factors from geologically relevant glass standards, with (first two columns) and without (last 2 columns) the NBS610 standard

	RSF	s.e	RSF (w/o NBS610)	s.e
$^{45}Sc/^{30}Si$	8.60E−03	1.42E−04	1.04E−02	2.91E−04
$^{86}Sr/^{30}Si$	1.09E−01	9.56E−03	1.18E−01	1.14E−02
$^{89}Y/^{30}Si$	2.30E−02	1.29E−03	4.82E−02	5.13E−03

The latter values were used to quantify our nanoSIMS analysis. RSFs determined by regression of secondary ion intensities for standard materials. Regression is forced through zero and s.e. is the standard error on the slope of the regression.

3. Results

The major element compositions (Table 1) of phases in the high pressure MORB assemblage (Figs. 1 and 3) are distinct from those produced in solid–melt partitioning experiments using an Al-depleted pyrolite, peridotite and chrondrite compositions at 25 GPa, 2300 °C (Hirose et al., 2004; Corgne et al., 2005; Liebske et al., 2005). The alumina content of magnesium silicate perovskites (*MgPv*) produced in *MgPv*–melt partitioning experiments is typically less than 0.13 Al pfu (atoms per formula unit), with Al assigned to the Si-site (Corgne et al., 2005; Liebske et al., 2005). The structural formula for the *MgPv* produced in our LH-DAC runs on the MORB assemblage is $(Mg_{.51}Fe_{.15}Al_{.23}Ca_{.06}Na_{.03})(Si_{.73}Al_{.27})O_3$, equivalent to ~40 mol% $AlO_{1.5}$ (Ricolleau et al., submitted for publication). This is significantly higher than that found in periclase-calcium ferrite saturated assemblages, ~25 mol% $AlO_{1.5}$, at pressures of 30–55 GPa (Walter et al., 2006), and could reflect increasing Al solubility in *MgPv* with increasing pressure. In this connection, a lower pressure (33 GPa) *CaPv–CF–St* saturated experiment (Ricolleau et al., submitted for publication) yields *MgPv* with an $AlO_{1.5}$ concentration equivalent to those of Walter et al. (2006). Calcium silicate perovskites (*CaPv*) from the LH-DAC experiments more closely resemble that from the Al-depleted pyrolite compositions at 25 GPa (Corgne et al., 2005), but with slightly higher iron concentrations — ~3.5 wt.% at 55 GPa versus concentrations below detection at 25 GPa.

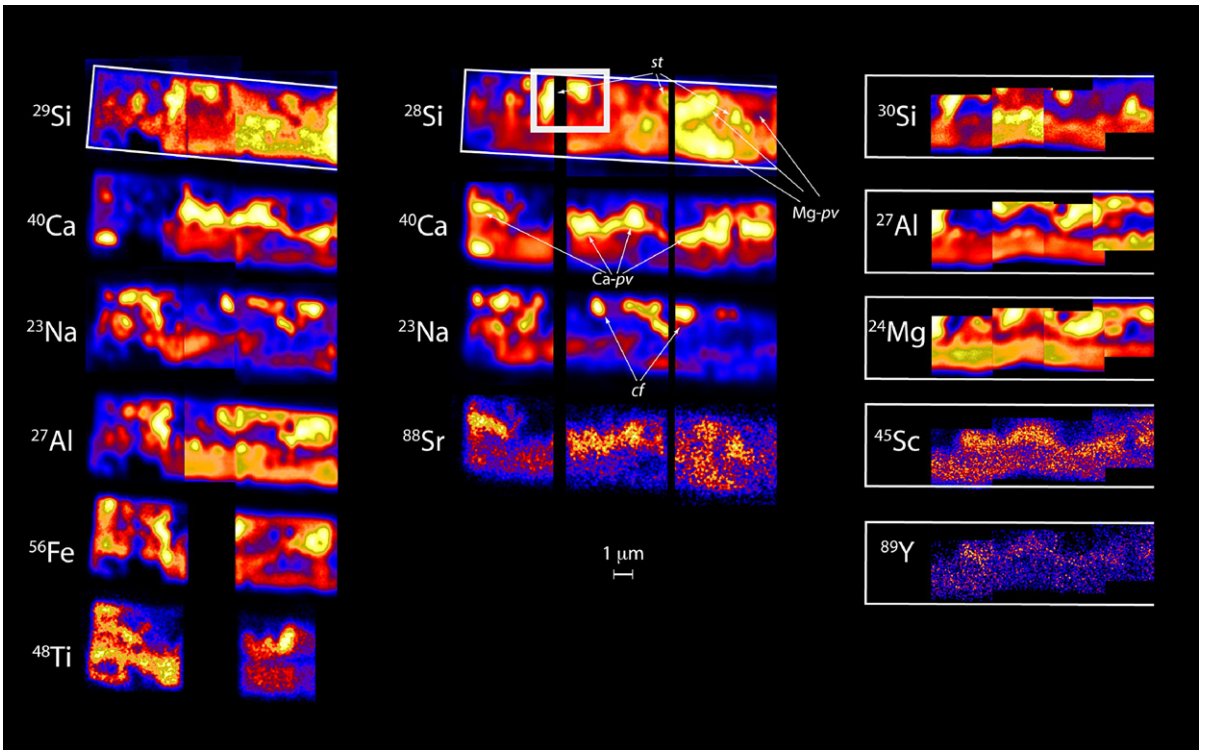

Fig. 3. Composite isotopic maps of a FIB slice taken from a LH-DAC-transformed natural fresh MORB. The isotopic images in the first two series (left and middle) are mosaics of three adjacent image areas. Individual grains can be distinguished by their characteristic chemical signature and are consistent with ATEM results. The ATEM image in Fig. 1 corresponds to the area outlined by the grey square in the middle panel. (Left) ^{29}Si, ^{40}Ca, ^{23}Na, ^{27}Al, ^{56}Fe images; the dark regions have not reached sputtering equilibrium. ^{48}Ti was probed subsequently, when the sample is closer to sputtering equilibrium. (Middle) A larger region, extending almost entirely across the FIB slice, is imaged using major elements and, ^{88}Sr. Strontium has a strong affinity for the *CaPv*, and is most depleted in stishovite. (Right) Higher resolution scan in the center of the sample. Three major elements are probed, along with ^{45}Sc and ^{89}Y. ^{45}Sc and ^{89}Y are close to the detection limit for these analytical conditions, however, it can be seen that ^{45}Sc and ^{89}Y follow the same trend as strontium, and partition preferentially into *CaPv* and are very depleted in stishovite.

A composite multi-isotope image of the FIB slice obtained for ^{23}Na, ^{24}Mg, ^{27}Al, ^{28,29,30}Si, ^{40}Ca, ^{56}Fe, ^{48}Ti, ^{45}Sc, ^{89}Y and ^{88}Sr using the NanoSIMS is shown in Fig. 3. As the NanoSIMS has a square raster pattern, the image of the rectangular FIB slice is a mosaic of 3 smaller images, each acquired in a given square area of the sample. The individual grains are clearly resolved in the major element maps, and can be identified as belonging to one of the four phases. The high spatial resolution of the oxygen beam allows the observation of grains on the order of 100 to 200 nm. *St*, *MgPv* and *CaPv* phases can be clearly identified from silicon, magnesium and calcium maps, respectively. The *CF* phase is more difficult to identify, and is characterized by higher aluminium and sodium content than other phases.

Trace element images for Sc, Y, and Sr were obtained for each phase and allow the partitioning of these elements within the assemblage to be quantified (Table 3). The accuracy of a particular measurement can be influenced by a number of experimental and analytical factors, *e.g.* spatial resolution *vs* grain size effects, in-depth variation in phase assemblage, and differences between the relative sensitivities factors between standards and unknowns. Given the small size of the phases of interest and the low concentrations of the analysed trace elements (40 ppm Sc and Y, 118 ppm Sr in the whole rock) some scatter in the

Table 3
Trace element concentrations (in ppm) in the mineral assemblage at 55 GPa and 2100 °C, obtained by nanoSIMS and mineral–mineral partition coefficients

	CaPv	S.D.	*MgPv*	S.D.	*St*	S.D.	*CF*	S.D.
Sc	54	10	24.5	2.1	6.7	0.7	3.1	0.4
$D^{min-MgPv}$	2.2	0.5			0.3	0.04	0.1	0.02
Sr	215	31	41	6	25	8	2.6	0.3
$D^{min-MgPv}$	5	1			0.6	0.2	0.1	0.01
Y	45	11	14	2	4.4	3.1	2.7	0.4
$D^{min-MgPv}$	3.1	0.9			0.3	0.2	0.2	0.04

Error of concentration data are given as one standard deviation (S.D.) propagating the error on the from population statistics and that associated with the regression of the relative sensitivity factors in Table 2.

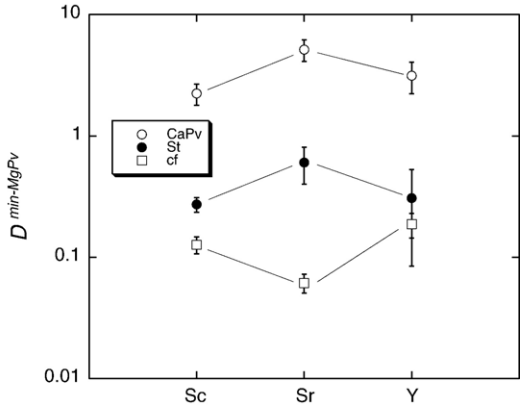

Fig. 4. Mineral–*MgPv* partition coefficients of Sc, Y, and Sr. The relatively flat pattern indicates mild inter-element fractionation, notably for *CaPv–MgPv*. This is a qualitative change with respect to fractionation at lower pressures (Fig. 5).

data is to be expected. Although the trace element concentrations sometimes lie near the detection threshold, the partitioning of these elements can be clearly observed in the images. For instance, it is clear that Sr, Sc, and Y partition preferentially into the *CaPv* phase and are depleted in all other phases, especially *CF* and *St*.

Twenty individual grains of *St*, *MgPv*, *CaPv*, and *CF* phase were isolated in the ion images and their Sc, Sr and Y concentrations determined (Table 3). The same RSF was used for each of the four silicate matrices as no systematic variation with major element composition was observed for the standard data, with the exception of NBS610. The trends observed visually in the ion images are confirmed by the quantitative analysis. Relative to *MgPv*, Sc, Sr and Y are enriched in *CaPv* but relatively depleted in *St* and *CF* (Fig. 4). In all cases, the patterns, relative to *MgPv* are relatively flat, displaying minor inter-element fractionation. Of particular interest is the partitioning of Sc, Sr and Y between *CaPv* and *MgPv*, as the relative abundance of these phases and their mineral–melt partitioning has been shown to play an important role in the chemical evolution of proposed terrestrial magma oceans (Hirose et al., 2004; Corgne et al., 2005; Liebske et al., 2005). The *CaPv–MgPv* partition coefficient for Sc is $D_{Sc}^{CaPv-MgPv}=2.2\pm0.5$ for Sr is $D_{Sr}^{CaPv-MgPv}=5\pm1$ and for Y is $D_{Y}^{CaPv-MgPv}=3.1\pm0.9$ (Table 3).

4. Discussion

A number of recent studies have investigated the partitioning of trace elements between perovskite and melts of peridotitic compositions (Hirose et al., 2004; Corgne et al., 2005; Liebske et al., 2005). However, the number of these investigations in which *MgPv* and *CaPv* coexisted is small. Hirose et al. (2004) have reported results from an experiment in which both *CaPv* and *MgPv* coexist with a melt of peridotitic composition at 2400 °C, 25 GPa (run LO#113), and $D^{CaPv-MgPv}$ for numerous trace elements can directly calculated from these results (Fig. 5). Corgne et al. (2005) report partition coefficients for $D_M^{CaPv-melt}$ and $D_M^{MgPv-melt}$, but *CaPv* (run H2020b) and *MgPv* (run H2020a) are not found in the same experiment and do not coexist with melts of exactly the same composition. The *CaPv–MgPv* partition coefficient, $D_M^{CaPv-MgPv}$, for element M can be related to the *Pv–melt* partition coefficients as,

$$D_M^{CaPv-MgPv} = D_M^{CaPv-melt}/D_M^{MgPv-melt} \quad (1)$$

if both phases are in equilibrium with the same melt. Combining the $D_M^{CaPv-melt}$ and $D_M^{MgPv-melt}$ results from different experiments reported by Corgne et al. (2005) is potentially problematic, as they have demonstrated that *Pv–melt* partition coefficients can vary with melt composition. However, one can attempt to circumvent this problem by restricting the discussion to trace element fractionation rather than absolute partitioning. A number of investigations of trace element partitioning between coexisting immiscible silicate melts demonstrate that melt structure and composition do not fractionate the REEs, Sc and Y (Watson, 1976; Ryerson and Hess, 1978; Ellison and Hess, 1989; Schmidt et al., 2006). Similarly, the

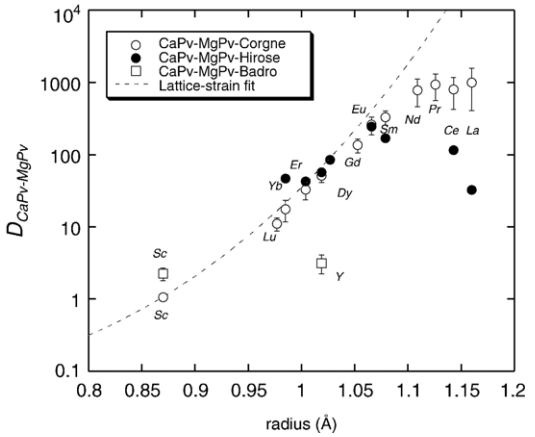

Fig. 5. *CaPv–MgPv* partition coefficients determined in (1) mineral–melt experiments by Hirose et al. (Hirose et al., 2004), (2) obtained by combining the results of 2 separate the multi-anvil (25 GPa) mineral–melt experiments by Corgne et al. (2005) and (3) by direct measurement of coexisting, subsolidus *CaPv* and *MgPv* at 55 GPa in the laser-heated diamond anvil cell (this study). The data are plotted as a function of ionic radius. The dashed line is the *CaPv–MgPv* partition coefficient obtained using the lattice strain parameters from the relevant experiments presented in Corgne et al. (2005).

inability of melt structure to fractionate cations of similar size and charge is one of the tenets of the lattice-strain mineral–melt partitioning model (Blundy and Wood, 1991). So while changes in melt composition will influence the absolute values of *Pv–melt* partition coefficients, the relative values (fractionation) among this group of elements should be essentially constant and relatively insensitive to changes in melt composition. Indeed, this is demonstrated by the similarity of $D_M^{CaPv-MgPv}$ obtained from the Hirose et al. (2004) and Corgne et al. (2005) results, which show the increasing compatibility of trivalent cations in *CaPv* with respect to *MgPv* with increasing ion radius (Fig. 5).

The *CaPv–MgPv* partitioning data obtained in ~25 GPa experiments involving relative Al-poor MgPv are quite different from those obtained here at higher pressures and substantially more Al-rich *MgPv* (Fig. 6). The *CaPv–MgPv* partition coefficients for Sr and Y in our 55 GPa are much lower than those in the obtained at 25 GPa. In addition, the fractionation of the large, trivalent cations, Sc and Y, is substantially reduced. As the composition of *CaPv* in all these experiments is relatively constant, these observations must be attributed to the changing composition, increased Al, in *MgPv*. When compared with the full suite of lanthanides (Fig. 5), suggests that increasing Al concentration in *MgPv* may make it more accommodating to trace element incorporation, but less effective in producing inter-element fractionation. One caveat required in the evaluation of these data concerns the effects of beam overlap and analytical spatial resolution. Beam overlap is essentially a mixing process, and in the extreme, all partitioning data tends toward unity. That some of the disparity observed between our data and the 25 GPa data originates from this process cannot be wholly discounted. However, the decreased inter-element fractionation is not so easily explained by this process, and would appear to be a reasonably robust observation.

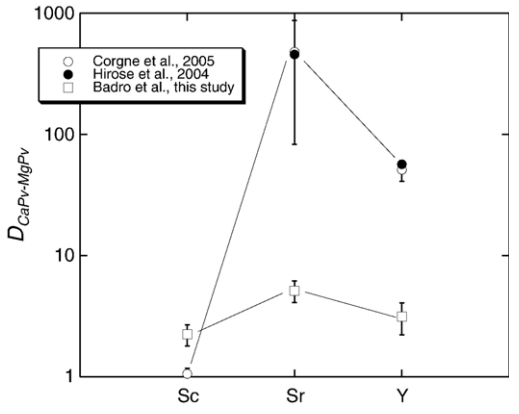

Fig. 6. A comparison of *CaPv–MgPv* partition coefficients determined at 25 GPa (Hirose et al., 2004; Corgne et al., 2005) and our coefficients determined at 55 GPa. The most notable effect of pressure is the flattening of the partition coefficient as a function of radius, indicating a reduced fractionation. We interpret this not so much as an intrinsic pressure effect, but rather as a consequence of the increased Al solubility in the *MgPv* structure at higher pressures.

The lattice-strain model of mineral–melt partitioning infers that the fractionation among the REEs will be controlled by the site modulus of the crystalline phase (Blundy and Wood, 1991), and in this connection, the observed decrease in Sc/Y fractionation and the inferred decrease in REE fractionation would require a decrease in that modulus of *MgPv* with increasing Al. Numerous workers have investigated the effect of Al incorporation on the bulk modulus of *MgPv* (Andrault et al., 2001; Jackson et al., 2004; Daniel et al., 2004; Walter et al., 2006). Walter et al. (2006) showed that Al is incorporated in *MgPv* by the charge-coupled mechanism, $Al+Al \Leftrightarrow Mg+Si$, in the pressure range 30–50 GPa, a mechanism consistent with the compositions of *CF*-saturated *MgPv* presented here and in Ricolleau et al. (submitted for publication) and with first principles calculations (Brodholt, 2000). While there are some inconsistencies in the bulk modulus vs. $AlO_{1.5}$ data, Walter et al. (2006) have defined a group of relatively high modulus measurements that show a mild decrease in modulus with increasing $AlO_{1.5}$. Extrapolating this trend to 40 mol% $AlO_{1.5}$ yields a bulk modulus of ~245 GPa, compared with 260–270 GPa for Al-free *MgPv*. Assuming that changes in the Young and bulk moduli are proportional, the decrease in bulk modulus expected as a function of increasing Al concentration is not alone sufficient to explain the apparent flattening of the large trivalent cation partitioning pattern we observe. Hence, we infer that the apparent 'flattening' of the REE partitioning pattern could be the product of local ordering with increasing Al-content, as recently suggested from calculations along the pyrope-grossular solid solution join (van Westrenen et al., 2003). The flattening could also be due to the increasing Al-REE coupled substitution; first principles calculations predict that the process of aluminium incorporation in perovskite changes at around 30 GPa, from an oxygen-deficiency mechanism at lower pressure to a charge-balanced mechanism at higher pressure (Brodholt, 2000) consistent with experimental observation between 30 and 50 GPa (Walter et al., 2006). These two scenarios could explain the difference in fractionation between that observed in our measurements, and those at lower pressures (Corgne et al., 2005; Liebske et al., 2005).

Fractional crystallisation of a terrestrial magma ocean has been suggested as a means of reconciling chondritic

and primitive upper mantle Mg/Si ratios with a combination of *CaPv* and *MgPv* constituting a hidden reservoir with subchondritic Mg/Si (Agee and Walker, 1988). Along with the relatively high Mg/Si ratios in Mg-perovskites from high-pressure mineral–melt experiments for peridotite compositions (Liebske et al., 2005) another observation arguing against significant perovskite fractionation is the non-chondritic trace element ratios predicted for the primitive upper mantle by geochemical models employing experimentally determined perovskite–melt partition coefficients (Kato et al., 1988; Hirose et al., 2004; Corgne et al., 2005; Liebske et al., 2005). For instance, based on data up to 25 GPa, only limited amounts of perovskite could be crystallised (~8%) while still maintaining the chondritic abundance of trivalent trace-element in the primitive upper mantle (Corgne et al., 2005). While the data are preliminary with no direct analysis of mineral–melt partitioning, the Al-enrichment in *MgPv* does decrease its ability to fractionate large trivalent cations while enhancing its overall capacity as a trace element host relative to *CaPv*. The effect would also influence *MgPv*–melt partitioning and may significantly decrease inter-element fractionation signature imposed by *MgPv–melt* fractionation, allowing higher amounts of perovskite fractionation. This preliminary experiment suggests that a more detailed experimental study of REE fractionation in the MgPv–CaPv system should be performed in the 20–50 GPa pressure range, to validate this hypothesis and to separate the effects of pressure and Al-concentration.

We have demonstrated that complex assemblages synthesized in the laser-heated diamond anvil cell in the conditions of Earth's lower mantle can be chemically imaged and analysed using state-of-the-art nanometer-scale secondary ion mass spectrometry (NanoSIMS). Analyses span a wide range of concentrations, from major, to minor, to trace elements. We have shown that Sc, Sr and Y have similar partitioning behaviour among the various phases (Mg and Ca silicate perovskites, stishovite and an aluminous phase) of transformed MORB up to 55 GPa and 2100 °C. Our preliminary results indicate a flattening of trivalent cation fractionation between *MgPv* and silicate liquid, suggesting that larger amounts of magma ocean crystallisation may be allowable, without disturbing the chondritic abundance for trace elements in the resulting primitive upper mantle. This class of experiments, that can be carried out on a variety systems, will help address issues ranging from early planetary differentiation and core formation (metal-silicate interactions), to the characterization of geochemical reservoirs in the lower mantle (solid–liquid silicate partitioning), and to the determination of the geochemical signature of lithospheric material subducted in the lower mantle and its influence on hotspot volcanism. These experiments extend the pressure and temperature range where trace element analysis can be accomplished, making the laser-heated diamond anvil cell an experimental petrology tool, and opening up a new field of research in deep-Earth geochemistry.

Acknowledgements

We thank Francis Albarède for fruitful discussions, and for comments on the manuscript. We acknowledge Christina Ramon for experimental help, and Guillaume Fiquet for discussions. This work was performed under the auspices of the U.S. Department of Energy by the University of California, Lawrence Livermore National Laboratory under contract No. W-7405-Eng-48 (UCRL-JRNL-228823), and was supported by the Laboratory Directed Research and Development Program (FJR) and the Basic Energy Sciences-Geoscience Research Program (PKW). This work was supported by the CNRS international relations directorate and by the INSU DyETI program (JB). JB acknowledges support from the University Relations Program at LLNL/University of California. *IMPMC* is UMR CNRS 7590. *IPGP* is UMR CNRS 7154.

References

Agee, C.B., Walker, D., 1988. Mass balance and phase density constraints on early differentiation of chondritic mantle. Earth Planet. Sci. Lett. 90, 144–156.

Andrault, D., Bolfan-Casanova, N., Guignot, N., 2001. Equation of state of lower mantle (Al,Fe)–$MgSiO_3$ perovskite. Earth Planet. Sci. Lett. 193, 501–508.

Badro, J., Fiquet, G., Guyot, F., Rueff, J.P., Struzhkin, V.V., Vanko, G., Monaco, G., 2003. Iron partitioning in Earth's mantle: toward a deep lower mantle discontinuity. Science 300, 789–791.

Badro, J., Rueff, J.P., Vanko, G., Monaco, G., Fiquet, G., Guyot, F., 2004. Electronic transitions in perovskite: possible nonconvecting layers in the lower mantle. Science 305, 383–386.

Blundy, J.D., Wood, B.J., 1991. Crystal-chemical controls on the partitioning of Sr and Ba between plagioclase feldspar, silicate melts, and hydrothermal solutions. Geochim. Cosmochim. Acta 55, 193–209.

Brandon, A.D., Walker, R.J., 2005. The debate over core–mantle interaction. Earth Planet. Sci. Lett. 232, 211–225.

Brodholt, J.P., 2000. Pressure-induced changes in the compression mechanism of aluminous perovskite in the Earth's mantle. Nature 407, 620–622.

Cliff, G., Lorimer, G.W., 1975. Quantitative-analysis of thin specimens. J. Microsc.-Oxford 103, 203–207.

Corgne, A., Liebske, C., Wood, B.J., Rubie, D.C., Frost, D.J., 2005. Silicate perovskite–melt partitioning of trace elements and geochemical signature of a deep perovskitic reservoir. Geochim. Cosmochim. Acta 69, 485–496.

Daniel, I., Bass, J.D., Fiquet, G., Cardon, H., Zhang, J.Z., Hanfland, M., 2004. Effect of aluminium on the compressibility of silicate perovskite. Geophys. Res. Lett. 31.

Ellison, A.J.G., Hess, P.C., 1989. Solution properties of rare-earth elements in silicate melts — inferences from immiscible liquids. Geochim. Cosmochim. Acta 53, 1965–1974.

Fiquet, G., 2001. Mineral phases of the Earth's mantle. Z. Kristallogr. 216, 248–271.

Heaney, P.J., Vicenzi, E.P., Giannuzzi, L.A., Livi, K.J.T., 2001. Focused ion beam milling: a method of site-specific sample extraction for microanalysis of Earth and planetary materials. Am. Mineral. 86, 1094–1099.

Hinton, R.W., 1990. Ion microprobe trace-element analysis of silicates — measurement of multielement glasses. Chem. Geol. 83, 11–25.

Hirose, K., Shimizu, N., van Westrenen, W., Fei, Y.W., 2004. Trace element partitioning in Earth's lower mantle and implications for geochemical consequences of partial melting at the core–mantle boundary. Phys. Earth Planet. Inter. 146, 249–260.

Irifune, T., Isshiki, M., Sakamoto, S., 2005. Transmission electron microscopy observation of the high-pressure form of magnesite retrieved from laser heated diamond anvil cell. Earth Planet. Sci. Lett. 239, 98–105.

Jackson, J.M., Zhang, J.Z., Bass, J.D., 2004. Sound velocities and elasticity of aluminous $MgSiO_3$ perovskite: implications for aluminum heterogeneity in Earth's lower mantle. Geophys. Res. Lett. 31.

Jochum, K.P., Dingwell, D.B., Rocholl, A., Stoll, B., Hofmann, A.W., Becker, S., Besmehn, A., Bessette, D., Dietze, H.J., Dulski, P., Erzinger, J., Hellebrand, E., Hoppe, P., Horn, I., Janssens, K., Jenner, G.A., Klein, M., McDonough, W.F., Maetz, M., Mezger, K., Munker, C., Nikogosian, I.K., Pickhardt, C., Raczek, I., Rhede, D., Seufert, H.M., Simakin, S.G., Sobolev, A.V., Spettel, B., Straub, S., Vincze, L., Wallianos, A., Weckwerth, G., Weyer, S., Wolf, D., Zimmer, M., 2000. The preparation and preliminary characterisation of eight geological MPI-DING reference glasses for in-site microanalysis. Geostand. Newsl.—J. Geostand. Geoanal. 24, 87–133.

Kato, T., Ringwood, A.E., Irifune, T., 1988. Experimental determination of element partitioning between silicate perovskites, garnets and liquids: constraints on early differentiation of the mantle. Earth Planet. Sci. Lett. 89, 123–145.

Liebske, C., Corgne, A., Frost, D.J., Rubie, D.C., Wood, B.J., 2005. Compositional effects on element partitioning between Mg-silicate perovskite and silicate melts. Contrib. Mineral. Petrol. 149, 113–128.

Madureira, P., Moreira, M., Mata, J., 2005. The Azores hotspot: a lower mantle origin for Terceira magmas as shown by Ne isotopic data. Geochim. Cosmochim. Acta 69, A106.

Murakami, M., Hirose, K., Kawamura, K., Sata, N., Ohishi, Y., 2004. Post-perovskite phase transition in $MgSiO_3$. Science 304, 855–858.

Reusser, E., Kägi, R., Gasser, P., Malmström, J., 2003. Focused ion beam technique as a preparation for chemical analysis at submicrometer scale. Geophys. Res. Abstr. 5.

Ricolleau, A., Fiquet, G., Addad, A., Menguy, N., Vanni, C., Perrillat, J.-P., Daniel, I., Cardon, H., Guignot, N., submitted for publication. Analytical transmission electron microscopy study of a natural MORB sample assemblage transformed at high pressure and high temperature, Am. Mineral.

Righter, K., 2003. Metal-silicate partitioning of siderophile elements and core formation in the early Earth. Ann. Rev. Earth Planet. Sci. 31, 135–174.

Ryerson, F.J., Hess, P.C., 1978. Implications of liquid–liquid distribution coefficients to mineral–liquid partitioning. Geochim. Cosmochim. Acta 42, 921–932.

Schmidt, M.W., Connolly, J.A.D., Gunther, D., Bogaerts, M., 2006. Element partitioning: the role of melt structure and composition. Science 312, 1646–1650.

Speziale, S., Milner, A., Lee, V.E., Clark, S.M., Pasternak, M.P., Jeanloz, R., 2005. Iron spin transition in Earth's mantle. Proceedings of the National Academy of Sciences of the United States of America, vol. 102, pp. 17918–17922.

Sturhahn, W., Jackson, J.M., Lin, J.F., 2005. The spin state of iron in minerals of Earth's lower mantle. Geophys. Res. Lett. 32.

Vancappellen, E., 1990. The parameterless correction method in X-ray-microanalysis. Microsc. Microanal. Microstruct. 1, 1–22.

Vancappellen, E., Doukhan, J.C., 1994. Quantitative transmission-X-ray microanalysis of ionic compounds. Ultramicroscopy 53, 343–349.

van Westrenen, W., Allan, N.L., Blundy, J.D., Lavrentiev, M.Y., Lucas, B.R., Purton, J.A., 2003. Trace element incorporation into pyrope-grossular solid solutions: an atomistic simulation study. Phys. Chem. Miner. 30, 217–229.

Walker, R.J., Morgan, J.W., Horan, M.F., 1995. Os-187 enrichment in some plumes — evidence for core–mantle interaction. Science 269, 819–822.

Walter, M.J., Tronnes, R.G., Armstrong, L.S., Lord, O.T., Caldwell, W.A., Clark, S.M., 2006. Subsolidus phase relations and perovskite compressibility in the system $MgO–AlO_{1.5}–SiO_2$ with implications for Earth's lower mantle. Earth Planet. Sci. Lett. 248, 77–89.

Watson, E.B., 1976. 2-liquid partition-coefficients — experimental-data and geochemical implications. Contrib. Mineral. Petrol. 56, 119–134.